Adaptive nonlocal quasicontinuum for deformations of curved crystalline structures

Jong Youn Park and Seyoung Im*
Department of Mechanical Engineering, Korea Advanced Institute of Science and Technology (KAIST), Science Town, Daejeon, Korea
(Received 12 November 2007; revised manuscript received 8 April 2008; published 14 May 2008)

This paper presents an adaptive multiscale simulation of deformations of curved crystalline structures such as carbon nanotubes (CNTs). It is based on quasicontinuum approach, which is a coarse-graining method. For fully nonlocal quasicontinuum, high-order interpolation functions are adopted to locate the deformed positions of atoms on a curved crystal structure. The "cluster" concept, which facilitates accurate energy approximation for crystals, is extended such that the vertices of elements or subdivided regions may be chosen irrespective of the positions of carbon atoms. Defining two remeshing criteria based on the second invariant of the Green's strain tensor and its gradient, an automatic adaptive scheme that provides gradually increasing resolution up to atomistic scale in nonlocal deformations of curved bodies is implemented. Various numerical examples, including a CNT fracture and deformations, demonstrate the effectiveness of the present scheme. This investigation realizes the adaptive simulation of nonlocal deformation for curved, as opposed to rectilinear, crystalline structures.

DOI: 10.1103/PhysRevB.77.184109 PACS number(s): 61.43.Bn, 61.46.Fg, 62.25.−g, 81.07.De

I. INTRODUCTION

The quasicontinuum method[1] has been widely applied to investigate the behaviors of defects, including dislocations as well as those associated with the grain boundaries and material interfaces of rectilinear crystalline bodies[2–4] at the atomistic level. The effectiveness of the quasicontinuum lies in the concurrent treatment of scales of different lengths between the local zone and the nonlocal zone, which assists with an investigation of the behaviors of various defects such as voids, twins, grain boundaries, and dislocations.[2,5–7] Due to this feature, the quasicontinuum method has attracted a substantial amount of attention as a computational methodology for multiscale boundary value problems in solid mechanics over the past decade. In particular, a fully nonlocal version of the quasicontinuum[8] paves the way for a seamless coupling approach without an additional treatment for inconsistency such as that known as ghost force[5] in the transition zone between the continuum and atomistic regions. However, most of the fully nonlocal versions of quasicontinuum have been limited to rectilinear crystalline bodies, and the extension of nonlocal quasicontinuum (QC) to curved crystalline structures has yet to be done to the best of the authors' knowledge.

This paper deals with a fully nonlocal quasicontinuum method for application to curved crystalline structures. A typical example of these curved crystalline structures includes carbon nanotubes (CNTs), for which the bulk of the relevant information is known due to the technological interest in these structures in relation to a variety of applications. For this reason, the focus here is on CNTs for curved crystalline structures.

Most studies have used molecular dynamics or atomistic model in order to look into the mechanics of nanotubes.[9–14] Moreover, many authors have employed a continuum or structural mechanics approach for more practical and efficient modeling.[15–20] Among others, Arroyo and Belytschko[15] reported a continuum model for curved crystalline sheets based on the exponential Cauchy-Born rule, which extends the standard Cauchy-Born rule to the case of curved crystalline structures. This was successfully applied to nonlinear mechanical deformations of multiwalled carbon nanotubes,[20] though its scope is limited to local behavior. A bridging scale[21] scheme between continuum and atomistic calculations has also been reported. This scheme enables the observation of local and nonlocal behaviors of CNTs through a single instantaneous simulation.[22] This is an excellent approach for multiscale simulations as long as the local zone and the nonlocal zone are known *a priori*. However, typically, multiscale problems are encountered for which the details or the size and range of the nonlocal zone that will develop are unknown. For rectilinear crystalline structures such as metals, an adaptive scheme combined with the quasicontinuum has been extremely successful in exploring various behaviors of defects in metals.[6–8] However, for curved crystalline bodies, there have been no studies reported thus far related to an automatic adaptive scheme with increasingly fine resolution up to atomistic scale.

In the present paper, an automatic adaptive computing scheme is reported for deformations of curved crystalline structures such as carbon nanotubes in the framework of the fully nonlocal quasicontinuum method.[8] The scheme seamlessly generalizes the standard quasicontinuum method to the case of a curved crystalline body in the sense that it enables one to deal with the nonlocal domain, i.e., the fully atomistic region, as well as the local domain, i.e., the coarse-grained region, for curved structures. A key feature includes the use of higher order interpolation functions to map curved geometries accurately and to interpolate the energy as well as the use of the cluster-weighted average of the interatomic potential energy to compute the force on the individual degrees of freedom. The outline of the paper is as follows. In Sec. II, the computational scheme is described, and this is followed by adaptive scheme in Sec. III and numerical examples in Sec. IV. Finally, Sec. V closes the paper with some concluding remarks.

II. QUASICONTINUUM FOR CRYSTALLINE BODIES

In this section, a method to extend the standard quasicontinuum for application to a crystalline body with curved geometry, such as a carbon nanotube, is discussed. The section starts with a brief summary of the quasicontinuum methods.

A. Overview of a nonlocal quasicontinuum

The total potential energy E_{total} of a given system is the summation of the individual potential energies E_i for all atoms in the system:

$$E_{total} = \sum_{i=1}^{N} E_i, \tag{1}$$

where N represents the total number of atoms in the system. The total energy E_{total} can be approximated by the coarse-grained energy E^h_{total} according to the node-based summation rule as follows:

$$E_{total} \approx E^h_{total} = \sum_{\alpha=1}^{N_R} w_\alpha E_\alpha. \tag{2}$$

Here, N_R indicates the total number of representative atoms, and w_α and E_α are the weight function and the potential energy, respectively, of the αth representative atom. In rectilinear crystalline structures, the mapping from the Lagrangian variable $\mathbf{X}_i$ to the current position $\mathbf{x}_i$ for the ith atom is approximated by $\mathbf{x}^h_i$, which is written in the form of the interpolation,

$$\mathbf{x}^h_i = \sum_{\alpha=1}^{N_R} S_\alpha(\mathbf{X}_i)\mathbf{x}_\alpha, \tag{3}$$

where $S_\alpha(\mathbf{X}_i)$ indicates the linear shape function associated with the αth representative atom, and $\mathbf{x}_\alpha$ denotes the current position of the αth representative atom or the nodal value in finite element (FE). Here, all variables $\mathbf{X}_i$, $\mathbf{x}_i$, $\mathbf{x}^h_i$, and $\mathbf{x}_\alpha$ indicate position vectors in the three-dimensional Euclidean point space. Assuming the interpolation of the energy distribution via the same function $S_\alpha(\mathbf{X}_i)$ gives

$$E^h_{total} = \sum_{i=1}^{N} \sum_{\alpha=1}^{N_R} S_\alpha(\mathbf{X}_i)E_\alpha. \tag{4}$$

A comparison of Eqs. (2) and (4) yields the following expression for the weight function:

$$w_\alpha = \sum_{i=1}^{N} S_\alpha(\mathbf{X}_i). \tag{5}$$

The preceding node-based summation rules are not free from the zero energy deformation modes. This, however, can be prevented by taking a sufficient number of sampling points.[8] In this context, this node-based summation rule is generalized to obtain what is known as a cluster-based summation rule,[8] in which the shape function is sampled not only at nodal points but also over neighborhoods, known as clusters, of the representative atoms. In this cluster-based method, each cluster plays the role of a node in the node-based rule; these are considered to be a representative crystallite over which the shape function values are sampled for interpolation. The coarse-grained energy according to the cluster-based rule is given as

$$E^h_{total} = \sum_{\beta=1}^{N_R} (w_\beta)_{cluster} \left[\sum_{i \in (cluster\ \beta)} E_i \right] \text{ with } E_i = \sum_{\substack{j \\ r_{ij} < r_{cut}}} E_i(r_{ij}), \tag{6}$$

where $(w_\beta)_{cluster}$ indicates the weight of the cluster summation rule. From Eqs. (4) and (6), it follows that

$$\sum_{\alpha=1}^{N_R} (w_\alpha)_{cluster} \sum_{i \in (cluster\ \alpha)} S_\beta(\mathbf{X}_i) = w_\beta, \tag{7}$$

where w_β is the weight function of Eq. (5) according to the node-based rule. Once $(w_\alpha)_{cluster}$ is obtained from this equation, it is straightforward to compute the nodal internal force by differentiating the coarse-grained potential energy of Eq. (6) so that the equilibrium configuration may be obtained. This is a fully nonlocal version of the quasicontinuum method, which maintains a smooth connection between the atomistic region and the continuum region and thus removes the interface between the two regions. This nonlocal scheme coarsens a domain without losing the atomistic framework and therefore furnishes seamless bridging between the fine and the coarse zones.[8] One of the striking features of this fully nonlocal method is that no explicit use of deformation measures such as deformation gradient and strain is made, even in the local zone, as opposed to the original quasicontinuum scheme by Tadmor *et al.*,[1] wherein deformation gradient or strain variables are employed to implement the constitutive equation in the local zone.

B. Deformations and inner displacements of carbon nanotubes

A graphene sheet, which is considered to be the given structure before the sheet is rolled into a tube, is a type of Bravais multilattice similar to a honeycomb structure. This lattice is composed of two simple triangular sublattices and is specified by two basis vectors $\mathbf{B}_1$ and $\mathbf{B}_2$ and a translational vector or shift $\mathbf{T}$, as shown in Fig. 1. Each atom site is reached by an integer multiple of two vectors $\mathbf{B}_1$ and $\mathbf{B}_2$ plus the shift vector $\mathbf{T}$ between the two sublattices. Under uniformly strained macroscopic deformations, the relative displacement between the two sublattices is an additional internal mode of deformation, not given by a homogeneous deformation field. The vector $\boldsymbol{\zeta}$ representing this additional mode of deformation (see Fig. 1) is termed the inner displacement between the two sublattices.[23,24] In the quasicontinuum method, for the sake of simplicity, it is essential to treat this additional deformation $\boldsymbol{\zeta}$ in the parental graphene domain, rather than in the deformed or current configuration. In the present section, we show that this is indeed possible. Our discussion is limited to the local zone, but it is valid in the nonlocal zone as well.

The undeformed reference configuration and current deformed configuration of a three-dimensional CNT are de-

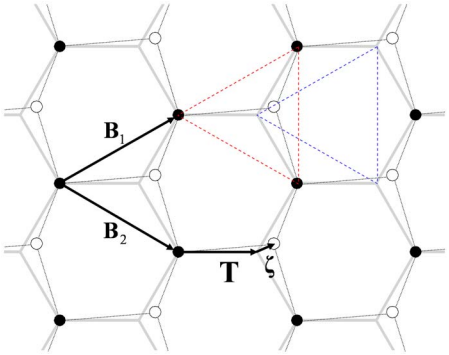

FIG. 1. (Color online) Inner displacement between two triangular sublattices comprising a graphene multilattice.

noted by $\mathbf{\Omega}_o$ and $\mathbf{\Omega}$ (see Fig. 2). Furthermore, their respective tangent planes $\bar{\mathbf{\Omega}}_o(\mathbf{X})$ and $\bar{\mathbf{\Omega}}(\mathbf{x})$ are defined at the undeformed position $\mathbf{X}$ and at the deformed position $\mathbf{x}$, respectively. The mapping from $\bar{\mathbf{\Omega}}_o(\mathbf{X})$ to $\mathbf{\Omega}_o$ and from $\bar{\mathbf{\Omega}}(\mathbf{x})$ to $\mathbf{\Omega}$ is given by exponential mapping.[25,26] Finally, the original configuration of the parental graphene sheet, i.e., the original configuration before it is rolled to $\mathbf{\Omega}_o$, is denoted by $\tilde{\mathbf{\Omega}}$, which may, strictly speaking, differ from $\bar{\mathbf{\Omega}}_o$ as the equilibrium bond distances may change due to curvature effects. Here, the superimposed "‾" indicates the tangent plane on three-dimensional tube while "˜" represents the plane in two-dimensional graphene.

It is assumed here that a homogeneous deformation $\mathbf{F}$ is imposed on an undeformed material line element belonging to the tangent space $\mathbf{T}_{\mathbf{X}}\mathbf{\Omega}_o$, which lies on the plane $\bar{\mathbf{\Omega}}_o(\mathbf{X})$. The resulting vector of the deformed material line element in this case belongs to the tangent space $\mathbf{T}_{\mathbf{x}}\mathbf{\Omega}$, which lies on $\bar{\mathbf{\Omega}}(\mathbf{x})$. At this point, $\varphi_o(\bar{\boldsymbol{\xi}}_o)$ may be contemplated as the exponential mapping[25,26] that transforms the tangent plane $\bar{\mathbf{\Omega}}_o$ onto the reference domain $\mathbf{\Omega}_o$ of the three-dimensional undeformed tube, where $\bar{\boldsymbol{\xi}}_o$ denotes a position vector on the tangent plane $\bar{\mathbf{\Omega}}_o$. Similarly, the transformation from the deformed tangent plane $\bar{\mathbf{\Omega}}$ into the current domain $\mathbf{\Omega}$ of the deformed tube may be described by another exponential mapping $\varphi(\bar{\boldsymbol{\xi}})$, where $\bar{\boldsymbol{\xi}}$ is a position vector on the tangent plane $\bar{\mathbf{\Omega}}$. For this, the position vector $\bar{\boldsymbol{\xi}}$ in the parental graphene domain has to be adjusted to account for the inner

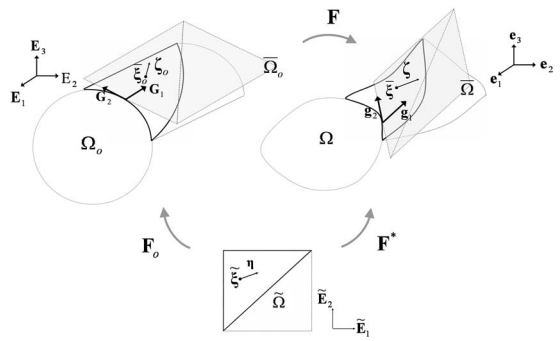

FIG. 2. Domains and deformation maps between the graphene and CNT tube.

displacement, and this is discussed in the subsequent paragraph.

As discussed earlier, the inner displacement $\boldsymbol{\zeta}$ is a supplementary deformation mode defined in the deformed domain $\bar{\mathbf{\Omega}}$. For convenience of development, the inner displacement $\boldsymbol{\eta}$ defined in the parental graphene domain $\tilde{\mathbf{\Omega}}$, which is related to $\boldsymbol{\zeta}$, is utilized, following Tadmor *et al.*[27] The position vector $\tilde{\boldsymbol{\xi}}$ of an atom in the parental graphene domain $\tilde{\mathbf{\Omega}}$ may be written as follows:

$$\tilde{\boldsymbol{\xi}} = m\mathbf{B}_1 + n\mathbf{B}_2 + (\delta - 1)\mathbf{T} \quad (\delta = 1 \text{ or } 2). \tag{8}$$

Here, m and n are integers and δ indicates sublattice 1 or 2. The position vectors $\bar{\boldsymbol{\xi}}_o$ and $\bar{\boldsymbol{\xi}}$ on each of the two tangent planes $\bar{\mathbf{\Omega}}_o$ and $\bar{\mathbf{\Omega}}$ are defined by the following relationships:

$$\bar{\boldsymbol{\xi}}_o = \mathbf{F}_o\tilde{\boldsymbol{\xi}}, \tag{9a}$$

$$\bar{\boldsymbol{\xi}} = \mathbf{F}\mathbf{F}_o\tilde{\boldsymbol{\xi}} + (\delta - 1)\boldsymbol{\zeta}. \tag{9b}$$

Here, $\mathbf{F}_o$ is a deformation gradient from the parental domain $\tilde{\mathbf{\Omega}}$ to the undeformed tangent plane $\bar{\mathbf{\Omega}}_o$ (see Fig. 2). The detailed expressions for the deformations $\mathbf{F}_o$ and $\mathbf{F}$ in Fig. 2 are described in the Appendix. The deformation $\mathbf{F}_o$ is nearly identical to the identity map; therefore, the shift vector taking place during $\mathbf{F}_o$ is neglected in Eq. (9a). The shift vector $\boldsymbol{\eta}$, referred to the parental domain $\tilde{\mathbf{\Omega}}$ of the original graphene sheet, then links to $\boldsymbol{\zeta}$ by the following relationship:

$$\boldsymbol{\eta} = (\mathbf{F}\mathbf{F}_o)^{-1}\boldsymbol{\zeta}. \tag{10}$$

Taking into account the inner displacement $\boldsymbol{\eta}$, the position vector $\tilde{\boldsymbol{\xi}}$ in the graphene domain is now adjusted to yield $\boldsymbol{\xi}$ as

$$\boldsymbol{\xi} = \tilde{\boldsymbol{\xi}} + (\delta - 1)\boldsymbol{\eta}, \tag{11}$$

where $\boldsymbol{\xi}$ is the position vector that is modified after taking into account the inner displacement in the graphene domain. Note that $\boldsymbol{\xi}$ and $\tilde{\boldsymbol{\xi}}$ are position vectors defined over the flat domain $\tilde{\mathbf{\Omega}}$ on the two-dimensional graphene and $\bar{\boldsymbol{\xi}}_o$ and $\bar{\boldsymbol{\xi}}$ are position vectors defined over the tangent plane $\bar{\mathbf{\Omega}}_o$ and $\bar{\mathbf{\Omega}}$ on the three-dimensional tube, respectively.

Once we establish Eq. (11), we may straightforwardly proceed to apply the nonlocal quasicontinuum method[8] for minimizing the total potential energy. As addressed at the end of Sec. II A, the nonlocal quasicontinuum approach directly computes the potential energy from the atomistic calculation without resorting to the use of any deformation variables such as deformation gradient $\mathbf{F}$ and other strain variables. Note that these deformation variables used to play a key role in implementing the elastic constitutive equation in the coarse-grained (local) zone in the case of the original quasicontinuum method.[1] In the nonlocal quasicontinuum scheme, however, the atomistic calculation of the total potential energy is implemented by way of the cluster-based approximation like Eq. (6) but with a higher order interpolation function to accurately trace the atom positions on a curved surface. The starting point toward this is to introduce a higher order interpolation referred to the parental graphene

domain $\tilde{\mathbf{\Omega}}$, and to represent the configurations in $\mathbf{\Omega}_o$ and $\mathbf{\Omega}$ in terms of $\boldsymbol{\xi}$. This is treated in the next section.

C. High-order interpolation for a curved crystalline structure

The kinematic constraint of the Cauchy-Born rule is imposed on the atomic configuration, and the crystalline bodies of carbon nanotubes are then tractable to the coarsening. Indeed, Arroyo and Belytschko[15] adopted the deformation gradient with respect to a graphene sheet and the local approximation of exponential mapping in order to acquire the information related to the atomic configuration. They successfully established a coarse-grained model based on continuum theory for a curved crystalline structure such as a carbon nanotube. In the present study, however, a higher order interpolation for the coarse graining of local zones subjected to the Cauchy-Born rule is introduced. Then, the total potential energy is directly calculated from this higher order interpolation of the atomic position vectors combined with the cluster-based summation rule, as will be shown in Sec. II D. For this, we first establish the higher order interpolation of the undeformed position vectors in $\mathbf{\Omega}_o$ and the deformed position vectors in $\mathbf{\Omega}$.

Here, $\boldsymbol{\xi}$ of Eq. (11) denotes the position vector or the Lagrangian coordinate with the inner displacement having been adjusted in the parental domain $\tilde{\mathbf{\Omega}}$ or the flat graphene sheet. The shape function describing deformation from $\tilde{\mathbf{\Omega}}$ to $\mathbf{\Omega}$ is now given as a function of $\boldsymbol{\xi}$. In this case, the atom position vector $\mathbf{x}$ in the current domain $\mathbf{\Omega}$ of a three-dimensional deformed tube as well as the position vector $\mathbf{X}$ in the reference domain $\mathbf{\Omega}_o$ of a three-dimensional undeformed tube cannot be written as in Eq. (3), as a linear shape function $S(\boldsymbol{\xi})$ fails to depict curved geometries. To represent a curved shell, quadratic interpolation at a minimum is required for the current position. The aforementioned observation at this point necessitates introducing higher order interpolations to contend with the curved geometry of carbon nanotubes. In terms of adaptability, triangular elements with the Hermite-type interpolation or a cubic Lagrange shape function pertaining to the area coordinates may be candidates. For convenience of modeling, the nodal points on the vertices of a triangular element can be chosen to coincide with the atom positions on the graphene. The mid nodes may not fall on atom sites in such a case. The nodes that fail to fall on an atom position, whether they are at vertices or at mid nodes, are termed here "atomless nodes" to distinguish them from the atom nodes (representative atoms in Sec. II A), of which the locations coincide with atom sites on the graphene. The choice of atomless sites for nodal points is made possible for the local zones by the Cauchy-Born rule, which leads to locally homogeneous deformations in the context of continuum mechanics.

For clarity, let $\mathbf{X}^v$ and $\mathbf{x}^v$ denote the position vector of a nodal point in the undeformed state $\mathbf{\Omega}_o$ and in the current domain $\mathbf{\Omega}$, respectively. These may be an atom node or an atomless node on the parental domain $\tilde{\mathbf{\Omega}}$ of the graphene sheet. Then, the current and the undeformed configurations, each of which is curved in nature, are represented by the following higher order interpolation:

$$\mathbf{X}_i^h = \sum_{\alpha=1}^{N_v} H_\alpha(\boldsymbol{\xi}_i)\mathbf{X}_\alpha^v \text{ and } \mathbf{x}_i^h = \sum_{\alpha=1}^{N_v} H_\alpha(\boldsymbol{\xi}_i)\mathbf{x}_\alpha^v. \tag{12}$$

Here, $\mathbf{X}_i^h$ and $\mathbf{x}_i^h$ are the three-dimensional interpolated position vector of the ith atom in the undeformed configuration and in the current configuration, respectively, and N_v is the total number of the nodal points for displacement or position interpolation. The function $H_\alpha(\boldsymbol{\xi})$ is a higher order shape function of αth node, which is defined on the position $\boldsymbol{\xi}$ of the graphene sheet, i.e., the parental domain $\tilde{\mathbf{\Omega}}$. This implies that all interpolation is taken with reference to the parental domain $\tilde{\mathbf{\Omega}}$. For the high-order interpolation, the cubic Lagrange interpolation function was chosen for the area coordinates employed in the finite element method.[28] The cubic Lagrange interpolation function turned out to be sufficient for describing deformed configurations of CNTs into generic curved shapes. Atoms on two-dimensional graphene can be mapped into an undeformed tube with a constant curvature vector or into a deformed tube with a varying curvature vector. As previously mentioned, this higher order mapping combined with the direct atomistic calculation based on the cluster-based scheme enables one to do without introducing deformation variables and the exponential mapping employed by Arroyo and Belytschko.[11] On the other hand, this high-order interpolation inevitably leads to atomless nodal points. In the absence of atoms on nodal points, it will likely be awkward to calculate the nodal energy in terms of Eq. (2), which is the approach of the original quasicontinuum with the node-based representation. However, the present approach with the cluster-based representation is capable of contending with the atomless nodes in the context of the locally homogeneous deformations, as long as the energy distribution is smooth enough to be tractable to interpolation. This is explained in the next section.

D. Coarse-grained energy and equilibrium equation of the system

At this point, the means of summing up the interatomic potential energies over the entire domain is considered. If the atom position $\mathbf{x}$ in the current domain Ω is interpolated by a high-order function, then the mid nodes of elements on the parental domain may not be located on the atom sites. It is important to note that the cluster-based rule [Eq. (6)] is capable of computing the energy of the cluster associated with a given node regardless of whether it is an atom node or an atomless node. Here, the cluster, which is considered to be a representative crystallite, possesses its energy even in the case of an atomless node. In addition, there are no difficulties in interpolating the field variables of the local zones as the locally homogeneous deformations prevail under the Cauchy-Born rule. If the interpolation function of the present high order (cubic) is chosen for the energy as well as for the deformed position vector field, the coarse-grained energy [Eq. (6)] is rewritten as

$$E_{total}^h = \sum_{\beta=1}^{N_v} (w_\beta)_{cluster} \left[\sum_{i \in cluster} \sum_{\beta}^{N_v} \sum_{\alpha=1} H_\alpha(\boldsymbol{\xi}_i) E_\alpha \right]. \tag{13}$$

The two weights w_α and $(w_\alpha)_{\text{cluster}}$ of a node and a cluster are then related according to

$$\sum_{\alpha=1}^{N_v} (w_\alpha)_{cluster} \sum_{i \in cluster} \sum_{\alpha} H_\beta(\boldsymbol{\xi}_i) = w_\beta. \tag{14}$$

Here, w_α is now defined as

$$w_\alpha = \sum_{i=1}^{N} H_\alpha(\boldsymbol{\xi}_i), \tag{15}$$

where the summation is taken over all of the atom sites within the support of the shape function $H_\alpha(\boldsymbol{\xi})$. The cluster prevents unexpected deformation by enriching the sampling points of energy. In addition, it diversifies the choice of the nodal points (vertex or mid nodes of the elements) regardless of the atom sites. Suppose a mesh changes from a coarse configuration to a fine configuration depending on the field gradient on the local region, and finally to fully atomistic or molecular mechanics (MM) model on the nonlocal zone. In the nonlocal zone, which is fully atomistic, the construction of clusters about the nodes in the nonlocal zone is not required. In other words, nodal point in the nonlocal zone is naturally identical to the atom point.

The constitutive equation for a local zone without external force is described in terms of the potential energy, which depends on the nodal vector $\mathbf{x}^v$ and the inner displacement $\boldsymbol{\eta}$:

$$\pi^h = \pi^h(\mathbf{x}^v, \boldsymbol{\eta}), \tag{16}$$

where the total potential energy π^h is nothing but total system energy E^h_{total}, given by Eq. (6), in the absence of external force. Note that $\boldsymbol{\eta}$ implicitly depends on the nodal position vector $\mathbf{x}^v$. Therefore, it is likely very complex and time consuming to find the minimum-energy configuration of potential [Eq. (16)] with respect to the nodal vector $\mathbf{x}^v$ and the inner displacement $\boldsymbol{\eta}$ at one time. Practically, an iterative search for the minimum-energy configuration is followed,[27] in which the variation of the potential energy is initially made to vanish with respect to the variation of $\boldsymbol{\eta}$ while $\mathbf{x}^v$ is held constant. The potential energy is then minimized with respect to $\mathbf{x}^v$ while $\boldsymbol{\eta}$ is held constant. This process is repeated until convergence is reached. Here, the superimposed hat "^" denotes a fixed value of $\mathbf{x}^v$ or $\boldsymbol{\eta}$. In this case, the former iterative step leads to the following equation:

$$\left.\frac{\partial \pi^h}{\partial \boldsymbol{\eta}}\right|_{\hat{\mathbf{x}}^v} = \left.\frac{\partial \pi^h}{\partial r_{ij}} \frac{\partial r_{ij}}{\partial \boldsymbol{\eta}}\right|_{\hat{\mathbf{x}}^v} = \left.\frac{\partial \pi^h}{\partial r_{ij}} \frac{\partial}{\partial \boldsymbol{\eta}} \left| \sum_{\alpha} [H_\alpha(\boldsymbol{\xi}_i) - H_\alpha(\boldsymbol{\xi}_j)] \hat{\mathbf{x}}^v_\alpha \right.\right| = 0. \tag{17}$$

In this equation, $\partial \pi / \partial r_{ij}$ is given in terms of $\partial E_i / \partial r_{ij}$ from Eq. (6), and i and j are atom numbers that ultimately determine the integers of basis vectors and the lattice number in Eq. (8). In Eq. (17), summation should be taken for the repeated indices i and j that meet $r_{ij} < r_{cut}$ within the given cluster. Additionally, $\boldsymbol{\xi}$ is related to the position vector $\tilde{\boldsymbol{\xi}}$ and the inner displacement $\boldsymbol{\eta}$ in the graphene domain, as in Eq. (11). The inner displacement $\boldsymbol{\eta}$, equivalent to the additional deformation referred to the original graphene plane, modifies the position of the atoms belonging to the second sublattice. The transformation from the original position vector $\tilde{\boldsymbol{\xi}}$ in the graphene sheet to the position vector $\boldsymbol{\xi}$ in consideration of the inner displacement eventually leads to the corresponding modification of the $H(\boldsymbol{\xi})$ value in Eq. (17). This implies that the mapping of each atom to the current configuration is discriminated according to the sublattice [$\delta=1$ or 2 in Eq. (8)] to which the atom belongs. It should be noted that the current configuration is constructed from the nodal position vector $\hat{\mathbf{x}}^v$ and the high-order interpolation function. At this point, the latter step serves to minimize the potential energy with respect to the nodal position vector $\mathbf{x}^v$ while maintaining the inner displacement at $\boldsymbol{\eta}=\hat{\boldsymbol{\eta}}$,

$$\frac{\partial \pi^h(\mathbf{x}^v, \hat{\boldsymbol{\eta}})}{\partial \mathbf{x}^v} = 0. \tag{18}$$

The inner displacement, which is uniform under homogeneous deformation, may be nonuniform, in general, in the subdivided region of the FE with a high-order interpolation function. It may be appropriate to consider another level of interpolation for the inner displacement that differs from the interpolation of the nodal position vector. However, for all numerical examples adopted in this study, it is sufficient to choose only one inner displacement vector within each element.

III. ADAPTIVE MESHING TECHNIQUE

For large deformations of complex domains, it is important to have the mesh to keep track of the deformation magnitude and the related gradient for the best possible simulation. If this is not done or possible, only *a priori* judgment can be relied on based on the qualitative characteristics of the deformation when constructing suitable meshes. In particular, this type of adaptive remeshing is important in coupling methods between continuum and atomistic calculations when a nanoscale system undergoes a surface effect. The implementation of a computational model for such automatic adaptation of a mesh demands a mesh generator for triangulation and an estimator for deformation. The code TRIANGLE was employed for the two-dimensional triangulation.[35] This code enables mesh generation with the constraint of the vertex, i.e., nodal points, lying on the graphene domain. To estimate the deformations, the deformation measure ε was chosen in the following process:[8]

$$\varepsilon = \sqrt{\mathrm{II}(\mathbf{E})} h/a. \tag{19}$$

Here, II, $\mathbf{E}$, h, and a are the second invariant of the strain, Green's strain, the element size, and the bond length or the lattice spacing in graphene, respectively. The strain $\mathbf{E}$ is simply obtainable according to its definition when the deformation gradients $\mathbf{F}$ defined in Fig. 2 is determined (see the Appendix). Note that $\mathbf{F}$ is obtained from $\mathbf{F}=\mathbf{F}^*\mathbf{F}_o^{-1}$ (see Fig. 2), where $\mathbf{F}^*$ and $\mathbf{F}_o$ are given by the gradient of $\mathbf{x}^v$ and $\mathbf{X}^v$ with respect to $\boldsymbol{\xi}$ with the aid of Eq. (12). For local zones, the Cauchy-Born rule suggests that atoms are displaced obeying the locally homogeneous deformation, which is the basic assumption of continuum mechanics. Then, each material element or atom locally deforms according to the polar decomposition $\mathbf{F}=\mathbf{RU}$ wherein $\mathbf{R}$ is associated with rigid rotation, so that it is sufficient to consider the stretch part, which is

directly linked to the second invariant of strain. If an element has a value of ε that is greater than a given tolerance, the element is refined with nodes that are added on the largest edge. However, it is necessary to have a mesh adapted for the gradient of deformation as well as for the magnitude of deformation so that a steep gradient of strains may be properly captured in the numerical solution. This is consistent with the basic premise for the coarse-grained local region, in which the deformation is free from any severe abrupt changes. Here, the gradient of deformation in the element subdomain is not constant, unlike the linear triangular element, due to the high-order element that is employed for the interpolation of the displacement field. The spatial derivative $\nabla\sqrt{\text{II}}$ of the square root of the second invariant II at the Gauss points of the high-order element is a good measure of the gradient of deformation. To approximate $\sqrt{\text{II}}$, the value of the jump of $\sqrt{\text{II}}$ across the interelement boundary for a specific element is initially calculated. This is essentially the difference of $\sqrt{\text{II}}$ between the two nearest Gauss points, each of which belongs to either of the two neighboring elements. Next, this is divided by the distance between the two corresponding Gauss points and is then averaged over the Gauss points considered for a given element. A more straightforward means of approximating $\nabla\sqrt{\text{II}}$ is to take the finite difference approximation between two neighboring Gauss points within a given element; this scheme essentially yields similar adaptive meshes. Before closing, the entire numerical procedure for computation is summarized below.

(1) Determine the position of atoms $\tilde{\boldsymbol{\xi}}$ on the graphene.

(2) Make elements data.

(a) Choose nodal points and make elements on the graphene by using mesh generator.

(b) Arrange the interpolation function $H(\boldsymbol{\xi})$ at initial position, $\boldsymbol{\xi}=\tilde{\boldsymbol{\xi}}$.

(3) Make undeformed tube data. (Exponential mapping is used for determining the initial undeformed tube from the graphene configuration. The initial tube with completely cylindrical structure has a constant curvature and unstretched tangential planes.)

(a) Determine the positions of nodes $\mathbf{X}^v$ on the undeformed tube initially of cylindrical shape.

(b) Represent the undeformed position $\mathbf{X}$ in $\mathbf{X}^v$ and $H(\boldsymbol{\xi})$ [see Eq. (12)].

(4) Minimize the energy π^h from the cluster-based approximation with respect to nodal point $\mathbf{x}^v$ and inner displacement $\boldsymbol{\eta}$. (This step is for finding the deformed atomic configuration, which is determined from the nodal values of the position vectors and the inner displacement. The incremental deformation is sought, starting from the undeformed state to find out a deformed configuration under a given loading or displacement. Note that the potential energy is computed directly from the given atomic potential, without resorting to the use of the deformation variables, and no exponential mappings are introduced for calculation of the deformed configurations.)

(a) Mimimize the energy with respect to $\boldsymbol{\eta}$ ($\partial\pi^h/\partial\boldsymbol{\eta}|_{\hat{\mathbf{x}}^v}=0$) while maintaining nodal position $\mathbf{x}^v=\hat{\mathbf{x}}^v$.

(b) Update the interpolation function $H(\xi)$ employing $\boldsymbol{\xi}=\tilde{\boldsymbol{\xi}}+\boldsymbol{\eta}$, where $\boldsymbol{\eta}$ is the new vector obtained above.

(c) Mimimize the energy with respect to $\mathbf{x}^v$ $[\partial\pi^h(\mathbf{x}^v,\hat{\boldsymbol{\eta}})/\partial\mathbf{x}^v=0]$ while maintaining the inner displacement $\boldsymbol{\eta}=\hat{\boldsymbol{\eta}}$.

(d) Update the nodal positions utilizing the new $\mathbf{x}^v$ obtained above and update $\mathbf{x}_i^h=\Sigma_{\alpha=1}^{N_v}H_\alpha(\xi_i)\mathbf{x}_\alpha^v$ [see Eq. (12)] for each of the reference and the current configuration.

(5) Calculate the deformation gradient $\mathbf{F}$ and the deformation measure ε.

(6) If $\varepsilon>$tolerance, then add nodal points on the longest edge of the element, and go to step (2). Else, update and save the nodal point and the inner displacement.

IV. NUMERICAL EXAMPLES

The Tersoff-Brenner interatomic potential[29,30] was chosen for the bonded interaction on the individual surface of carbon nanotubes, and the Lennard-Jones type potential[31] was chosen to represent the nonbonded interaction between neighboring walls. The role of this nonbonded potential is very important when rippling or buckling occurs such that the tube wall may come into van der Waal's contact.[20] For minimization, limited memory BFGS,[32,33] which is known as an efficient quasi-Newton method, was adopted.

A. Cluster radius study

For a large-scale simulation, it is not efficient to calculate the energies of clusters containing a large number of atoms. An example of bending is used to examine the influence of the size of the cluster radius on the calculation of the potential energy. A 43.36 nm long (60,0) single walled carbon nanotube (SWCNT) is used in this examination. The entire domain of the tube is modeled with a total 368 elements with cubic shape functions. Refinement is not adopted during the simulation, but a uniform mesh is chosen, as the focus here is on looking into the effect of the cluster size on the accuracy of the solution. There are 24 000 atoms overall, which amounts to a total number of degrees of freedom of 72 000. The total number of degrees of freedom in the QC model is 5776, which is approximately 8% of that in the MM model. A bending condition is imposed by displacement on each end of the tube, and the imposed bending angle ranges from 0° to 15°. If the cluster radius is greater than 4.45 Å, which is approximately three times the bond length of the graphene ($r_o=1.45$ Å), the boundaries of any two neighboring clusters meet over the entire domain for this mesh. The strain energy is calculated for each of the different values of cluster radius [see Fig. 3(a)]. Figure 3(b) shows the strain energy trend zoomed in near the buckling point. Figure 3(c) shows the relative errors in the strain energies with respect to the cluster radii, given in multiples of the bond length r_o of the graphene before and after the buckling point. The reference value E_r denotes the strain energy of the model with the largest cluster radius ($r_o=1.45$ Å).

The energy of an atom on the free-edge boundary [free surface in three-dimensional (3D) bulk system] is higher than the energy of an atom in the bulk of the interior due to bond termination. According to the Brenner potential for a carbon system, for example, an atom on the boundary and

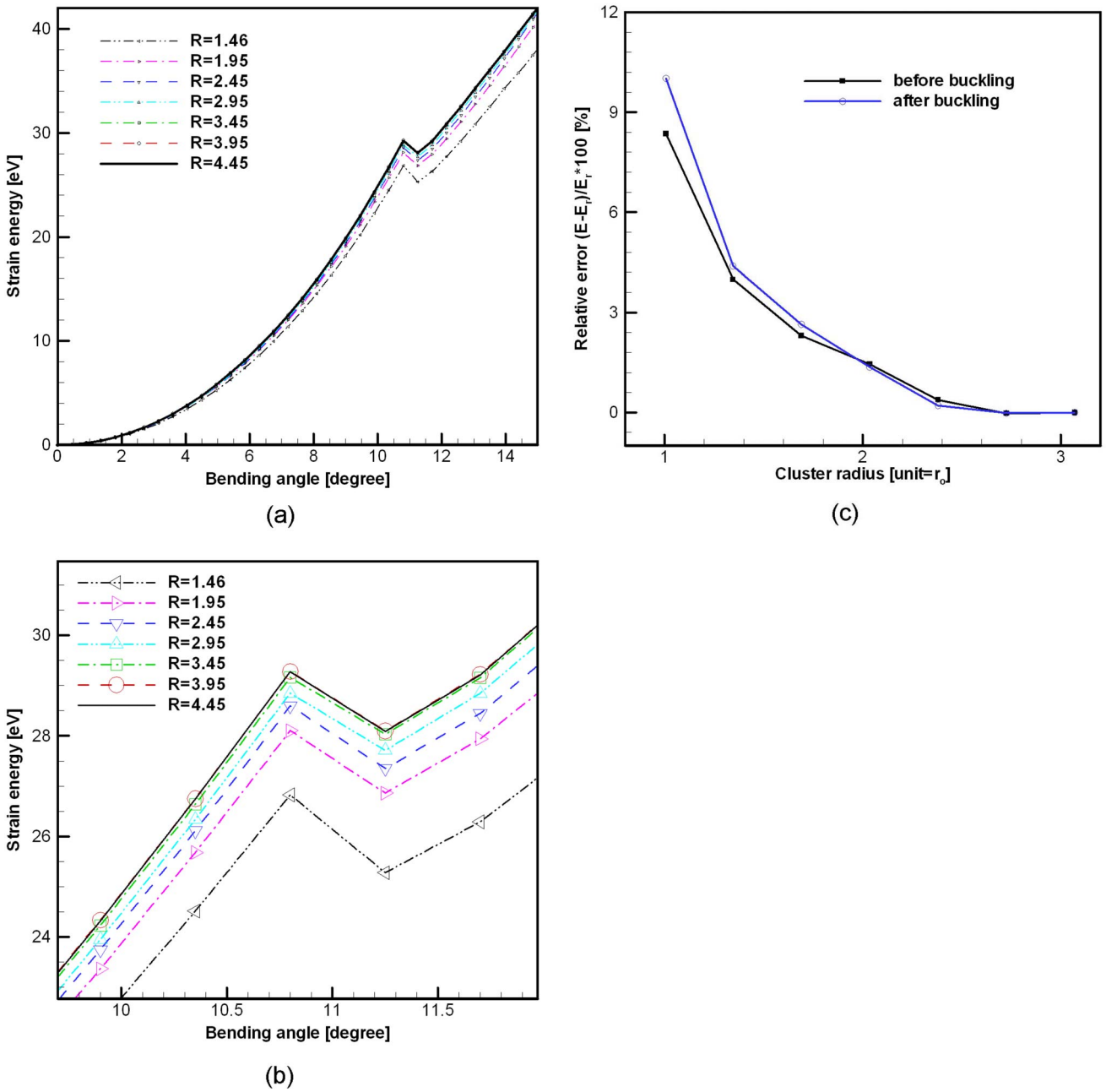

FIG. 3. (Color online) Cluster radius study in a bending simulation of a SWCNT: (a) strain energy curves with respect to the bending angle according to various cluster radii, (b) strain energy curves zoomed in near the buckling point, and (c) relative errors of the strain energy versus cluster radii before and after the buckling point.

one in the interior layer next to this boundary has an energy gap of approximately 2 eV in the case of CNTs. This gives rise to a substantial amount of difference in the total energy over the entire domain, depending on the size of the cluster radius. In other words, the energies associated with atoms on the free surface may not be accurately reflected in coarse graining, particularly if the mesh is not refined well enough to capture the localized nature near the free surface boundary. This influence of the edge atoms is termed the "edge effect" (or the "surface effect" for a 3D bulk system). Two cases, the first for the smallest cluster radius (1.46 Å) and the second for the largest cluster radius (4.45 Å), yield a 4.96% energy gap for each node lying on the edge of the tube (about a 127 eV gap in total energy for this model). This will clearly affect the local equilibrium near the free surface, and full atomistic scale refinement or at least the maximum cluster radius in the case of coarsening is necessary to capture the localized deformation near the free surface. However, the strain energy, which is defined as the difference of the overall energy levels between the initial and the final configurations, is much less sensitive to the size of the cluster radius, as the energy deviation due to the free surface has been subtracted. The instability point links to the strain energy, which is mostly invariant with respect to the change of the size of the cluster radius, as shown in Fig. 3(a).

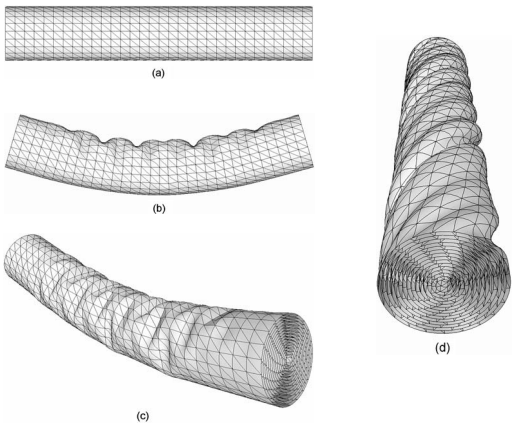

FIG. 4. Bending [(b) and (c)] and twisting (d) simulations for a 15-walled CNT: (a) front view of the initial configuration, (b) a front view, (c) a perspective view of equilibrium configuration at the bending angle 34°, and (d) a perspective view of the equilibrium configuration at the twisting angle of 130°.

B. Deformation of multiwalled carbon nanotubes

A large-scale simulation was conducted in order to demonstrate the efficiency of the proposed coarse-grained scheme. A 15-walled carbon nanotube with a length of 62.54 nm and a diameter of 11.08 nm is used in a simulation of bending [see Fig. 4(a)]. The chiralities from the inner wall to the outer wall are (10,10), (15,15), …, (80,80). This multiwalled CNT containing 673 650 atoms has over 2×10^6 degrees of freedom. The QC model used in this simulation consists of 291 244 degrees of freedom, which is less than 13% of the fully atomistic calculations. In this system, the entire domain is subdivided into the QC zone. The cluster radius is 2.0 Å, which is approximately 48% of the maximum radius. Bending and twisting motion is applied by imposing displacement on both (respective) ends of the tube, with an imposed bending angle ranging from 0° to 34° and a twisting angle ranging from 0° to 130°. At the final step of bending angle, the CNT reaches a deformed state in three-dimensional buckles. Although the system in this case is smaller in size compared to those observed by Poncharal *et al.*,[34] this deformation agrees very well with the rippling structure reported in experiments[34] and in simulations.[20] The ripples shown in Fig. 4(b) were built by sequences of simple two buckles on top and two tilted buckles on the side [see Fig. 4(c)].[20] The equilibrium configurations in the twisting simulation show inhomogeneous deformation, i.e., rippling, which is similar to the bending case.

C. Numerical examples using the adaptive scheme

Before looking into remeshing examples, it is necessary to consider what is known as the boundary effect in the adaptive meshing simulation. The "boundary effect" is defined as the influence of the boundary condition during the refinement of the mesh. This boundary effect is different from the edge effect in Sec. IV A. The edge effect was previously examined; the cluster-based energy calculation was determined to overestimate the total energy due to high-energy

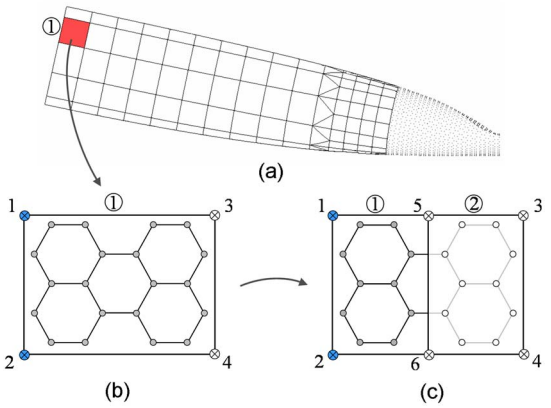

FIG. 5. (Color online) Boundary effect caused by refinement in coarse graining: The circles indicate atom sites, and the crossed circles indicate nodal points. The states of energies associated with the atoms at the gray circles are affected by the boundary condition, which is represented by the boundary nodes at the crossed blue circles; the energies of the atoms at the open circles are free from imposed constraint. (a) Half of a bent tube with the displacement boundary condition imposed on the end, (b) one-element case on a prescribed boundary region before refinement, and (c) two-element case after refinement.

atoms on the fee edge of the tube while not affecting the strain energy. This effect vanishes when the cluster radius increases to its maximum, even if the full atomistic refinement is not yet taken. In other words, if the clusters cover the entire domain, the total energy of the system is precisely calculated within the accuracy of the geometry interpolation by the shape function for all atoms regardless of whether refinement takes place or not. Tadmor *et al.*[1] found that the free surface (or edge), which is one of the interfacial effects, can be captured by nonlocal QC formulation. In contrast to the edge effect, the boundary effect appears even if the cluster radius has the maximum value. To illustrate this, two elements are depicted. They represent conditions before and after refinement leading to subdivision of element 1 into elements 1 and 2 on an edge of a bent tube, as shown in Fig. 5(a). Figure 5(b) shows a four-node quadrilateral element and atoms belonging to the element. The displacement boundary condition for bending is imposed on nodes 1 and 2 on the edge but not on nodes 3 and 4 in the interior. As the positions of atoms belonging to the element are interpolated by the nodal positions, the atoms are directly constrained by the fixed boundary conditions of nodes 1 and 2 during the minimization step at a specific bending angle. This implies that the system becomes stiffer as the mesh continues to coarsen; therefore, the atoms bound by this crude interpolation lie in a higher energy state under prescribed displacement boundary conditions. Assuming that the element is divided into two elements 1 and 2 via refinement, as shown in Fig. 5(c), the atoms in element 2 are then no longer affected by nodes 1 and 2 under the displacement boundary condition. Therefore, the bound atoms of element 2 before refinement are now free from their constrained condition, and the strain energy of the system is relaxed. Under the traction boundary condition, the opposite phenomenon will take place. Consistent with this observation, the adaptive compu-

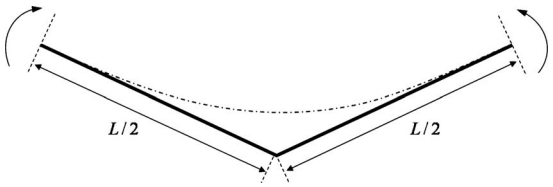

FIG. 6. Bending plus compression of the CNT under consideration (L=the initial length of the CNT). The dashed-dotted line indicates the centroidal line of the tube in the deformed configuration.

tation here indicates that the region in which the boundary condition is imposed is modeled as fully atomistic and that this is capable of properly accounting for the boundary effect.

The first example considered for the adaptive meshing scheme is a bending simulation of a 52.34 nm long (40,40) armchair SWCNT. The bending plus compression is imposed by prescribing the positions of the atoms on each cross section of the two ends and is schematically described in Fig. 6. This tube contains 33 360 atoms, implying that the total number of degrees of freedom for the fully atomistic simulation is 100 080. The displacement boundary condition is imposed on two edges of the tube, as in the previous models. The initial QC model has only a local zone composed of 192 elements with a cubic shape function. While finding the equilibrium at the bending angle of 0°, it is observed that the QC model is refined around both of its ends for the accurate estimation of the strain energy due to the presence of the boundary effect. The total number of degrees of freedom in this case reaches 13 150 (see Fig. 8). The criterion for refinement of the mesh is 0.07 for the deformation measure defined in Eq. (19) and $0.005a$ for its derivative $a\nabla\sqrt{\Pi}$. We have employed the cluster radius of 2.5 Å, which is 50% of the maximum radius in the initial mesh on the graphene. Starting from a bending angle 4.2°, refinement takes place from the upper surface on the tube in the middle of its length. The center of the tube where the kink occurs is characterized by nearly complete atomistic resolution. Then, at 8.8° and at 9°, which correspond to just before and directly after kinking, the degrees of freedom are 21 973 and 29 324, respectively. At the final bending angle of 18°, the total number of degrees of freedom is 31 807, which is 31.8% of that required in MM. The strain energy curve is shown in Fig. 7. The relative error of the QC model in the strain energy, compared with MM model, is 1.4% and 3.5% at angles of 8.8° and 9°, respectively. Despite the smaller number of degrees of freedom compared to the MM model, the QC model is able to predict the instability point accurately in the bending simulation. Figure 8 shows deformed configurations of the atoms and meshes at bending angles of 0°, 8.8°, 9°, and 18°. A visualization of the deformation of the CNT and of its adaptive meshing shown in Fig. 8 is available online.[36]

The quasicontinuum is a concurrent multiscale method that couples the atomistic scale with the continuum scale. Therefore, this method is able to capture the atomistic features, e.g., defects and bond breakage or bond creation within the range of accuracy of the interatomic potentials employed in the nonlocal region. To demonstrate this aspect,

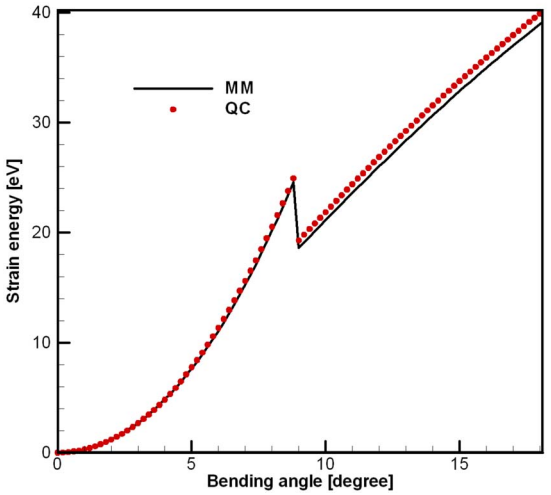

FIG. 7. (Color online) Strain energy versus the bending angle in a QC simulation using adaptive meshing.

tensile simulation for the fracture of a CNT with an initial defect in the form of vacancy is examined, as in a related bending case. The chirality is (24,24) and the length of the model is 16.32 nm. The model is considered to have a 12-atom vacancy, i.e., two hexagons are removed from the CNT. The fully atomistic or MM model has 18 828 degrees of freedom. The displacement boundary condition is imposed at both ends. Instead of the cutoff function in the original potential,[30] which is not appropriate for a fracture mechanism, the bond list is constructed using the original cutoff distance (2.0 Å) in the initial configuration for the tensile

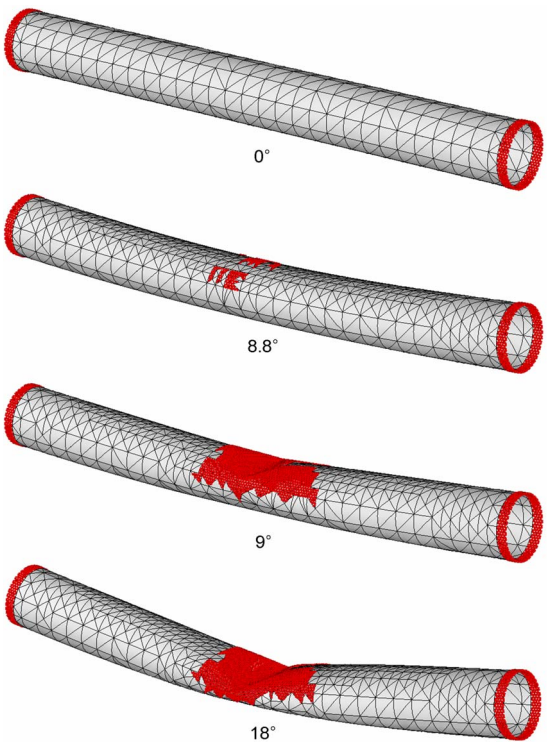

FIG. 8. (Color online) Equilibrium configurations of atoms and meshes at each bending angle.

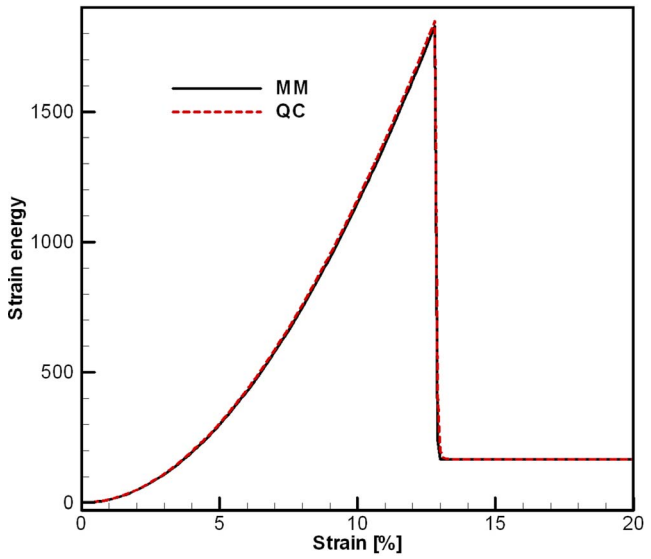

FIG. 9. (Color online) Strain energy curve versus strain in tensile simulation using adaptive meshing.

simulation of the fracture.[37] Figure 9 shows the strain energy versus the strain; the abrupt collapse of the strain energy is caused by the sudden relaxation due to the fracture propagated throughout the entire CNT cross section. As shown in Fig. 9, the fracture strains of the MM model and the QC model are in excellent agreement. The fracture strain is approximately 0.128 and the nominal stress at the point of failure is approximately 73 GPa. The stress is simply determined by dividing the total cross-sectional force on the atoms at the end by the cross-sectional area of the tube. The area of the cross section is given by πDt, where D is the diameter of the CNT and t is the thickness, which is taken to be the interlayer distance 0.345 nm in graphite. This is close to the distance based on the van der Waals radius. This fracture stress is smaller than that of a pristine tube. The decrease in the strength is attributed to the role of the defect in the fracture of a CNT.[38] The QC model, which initially started with 7959 degrees of freedom, eventually attains 9955 degrees of freedom at the moment of fracture (see Fig. 10). A visualization of the deformation of the CNT and its adaptive meshing for the tensile model is also available online.[36] This example clearly demonstrates the strength of the present multiscale scheme of computation; this study enables an adaptive computation for curved crystalline bodies.

Before closing this section, it is important to note that the preceding example of a CNT fracture is dependent on the quality of the force field employed for its accuracy. The atomistic model using an empirical potential such as Tersoff-Brenner is not as accurate as a tight-binding model or an *ab initio* calculation when a configuration of atoms substantially deviates from equilibrium. For accurate computations, multiscale computing, in which a quantum mechanical zone is taken around the void while the remaining area is modeled as QC, should be employed. This is currently ongoing and will be reported in a subsequent publication.

V. CONCLUSION

In this paper, a simple method of extending a conventional QC to the case of a curved crystalline body such as a CNT is proposed. The concept of atomless degrees of freedom is introduced, which makes it possible to employ higher order interpolations for the position and displacement vectors in a cluster-based QC. This enables treatment of nonlocal zones as well as local zones in deformations of curved crystalline sheets. The present method combined with an adaptive scheme based on the gradient of deformation as well as the magnitude of deformation assures accurate results regardless of the initial model. Various numerical examples demonstrate the accuracy and the effectiveness of this method.

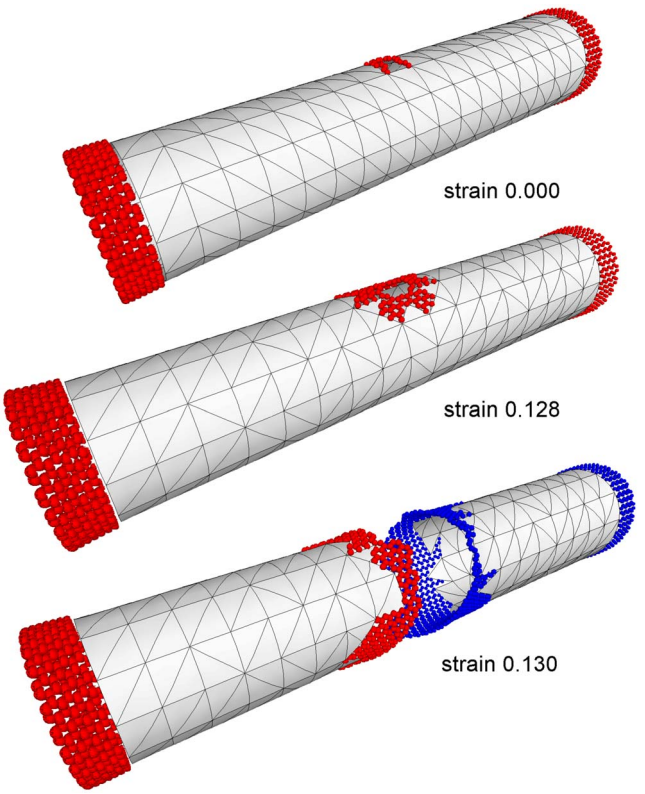

FIG. 10. (Color online) Equilibrium configurations of atoms and meshes at each tensile strain: Each of the split pieces is colored differently after the fracture.

ACKNOWLEDGMENTS

This research was supported by a Korea Science and Engineering Foundation (KOSEF) grant funded by the Korean government (MOST) (R0A-2007-000-20115-0).

APPENDIX

Let $d\mathbf{X}$ and $d\mathbf{x}$ denote infinitesimal vectors on each of the two configurations Ω_o and Ω of three-dimensional tube, respectively (see Fig. 2), and write as follows:

$$d\mathbf{X} = dX^i \mathbf{E}_i = d\chi^\alpha \mathbf{G}_\alpha, \tag{A1}$$

$$d\mathbf{x} = \mathbf{F} d\mathbf{X} = dx^i \mathbf{e}_i = d\phi^\alpha \mathbf{g}_\alpha, \tag{A2}$$

where $\mathbf{E}_i$ and $\mathbf{e}_i$ $(i=1,2,3)$ are basis vectors of domains Ω_o and Ω in three dimension, respectively, and $\mathbf{G}_\alpha$ and $\mathbf{g}_\alpha$ $(\alpha$

$=1,2$) are defined as convected base vectors on the surface of the undeformed and deformed tube, respectively. In the same context, infinitesimal material vector $d\boldsymbol{\xi}$ on the parental domain $\tilde{\Omega}$ of the two-dimensional graphene sheet is written in basis vector $\tilde{\mathbf{E}}_\alpha$ as follows:

$$d\boldsymbol{\xi} = d\xi^\alpha \mathbf{E}_\alpha = d\xi^1 \tilde{\mathbf{E}}_1 + d\xi^2 \tilde{\mathbf{E}}_2. \tag{A3}$$

Then, the deformation gradients $\mathbf{F}_o$ and $\mathbf{F}^*$ from the graphene sheet $\tilde{\Omega}$ to undeformed tubes Ω_o and from the graphene sheet $\tilde{\Omega}$ to the deformed tube Ω are written as, respectively,

$$\mathbf{F}_o = \frac{\partial \mathbf{X}}{\partial \boldsymbol{\xi}} = \frac{\partial X^i}{\partial \xi^\alpha} \mathbf{E}_i \otimes \tilde{\mathbf{E}}^\alpha = \frac{\partial \chi^\beta}{\partial \xi^\alpha} \mathbf{G}_\beta \otimes \tilde{\mathbf{E}}^\alpha \quad (2 \times 2 \text{ matrix}), \tag{A4}$$

$$\mathbf{F}^* = \frac{\partial \mathbf{x}}{\partial \boldsymbol{\xi}} = \frac{\partial x'}{\partial \xi^\alpha} \mathbf{e}_i \otimes \tilde{\mathbf{E}}^\alpha \quad (3 \times 2 \text{ matrix}). \tag{A5}$$

Finally, the deformation $\mathbf{F}$ from the graphene sheet Ω_o to deformed tube Ω is given as follows:

$$\mathbf{F} = \mathbf{F}^* \mathbf{F}_o^{-1} = \left(\frac{\partial x^i}{\partial \xi^\alpha} \mathbf{e}_i \otimes \tilde{\mathbf{E}}^\alpha \right) \cdot \left(\frac{\partial \xi^\beta}{\partial \chi^\delta} \tilde{\mathbf{E}}_\beta \otimes \mathbf{G}^\delta \right). \tag{A6}$$

*Author to whom correspondence should be addressed; sim@kaist.ac.kr

[1] E. B. Tadmor, M. Ortiz, R. Phillips, and R., Philos. Mag. A **73**, 1529 (1996).
[2] R. Miller, M. Ortiz, R. Phillips, V. Shenoy, and E. B. Tadmor, Eng. Fract. Mech. **61**, 427 (1998).
[3] V. B. Shenoy, R. Miller, E. B. Tadmor, R. Phillips, and M. Ortiz, Phys. Rev. Lett. **80**, 742 (1998).
[4] V. B. Shenoy, R. Phillips, and E. B. Tadmor, J. Mech. Phys. Solids **48**, 649 (2000).
[5] V. B. Shenoy, R. Miller, E. B. Tadmor, D. Rodney, R. Phillips, and M. Ortiz, J. Mech. Phys. Solids **47**, 661 (1998).
[6] J. Knap and M. Ortiz, Phys. Rev. Lett. **90**, 226102 (2003).
[7] J. Marian, J. Knap, and M. Ortiz, Phys. Rev. Lett. **93**, 165503 (2004).
[8] J. Knap and M. Ortiz, J. Mech. Phys. Solids **49**, 1899 (2001).
[9] S. Iijima, C. Brabec, A. Maiti, and J. Bernholc, J. Chem. Phys. **104**, 2089 (1996).
[10] B. I. Yakobson, Appl. Phys. Lett. **72**, 918 (1998).
[11] T. Belytschko, S. P. Xiao, G. C. Schatz, and R. S. Ruoff, Phys. Rev. B **65**, 235430 (2002).
[12] M. Huhtala, A. Kuronen, and Kimmo Kaski, Comput. Phys. Commun. **147**, 91 (2002).
[13] Y. Shibutani and S. Ogata, Modell. Simul. Mater. Sci. Eng. **12**, 599 (2004).
[14] P. Liu, Y. W. Zhang, H. P. Lee, and C. Lu, Mol. Simul. **30**, 15 (2004).
[15] M. Arroyo and T. Belytschko, J. Mech. Phys. Solids **50**, 1941 (2002).
[16] X.-L. Gao and K. Li, Int. J. Solids Struct. **40**, 7329 (2003).
[17] A. Pantano, D. M. Parks, and M. C. Boyce, J. Mech. Phys. Solids **52**, 789 (2004).
[18] L. Nasdala, G. Ernst, M. Lengnick, and H. Rothert, Comput. Model. Eng. Sci. **7**, 293 (2005).
[19] H. W. Zhang, J. B. Wang, and X. Guo, J. Mech. Phys. Solids **53**, 1929 (2005).
[20] M. Arroyo and T. Belytschko, Phys. Rev. Lett. **91**, 215505 (2003).
[21] D. Qian, G. J. Wagner, and W. K. Liu, Comput. Methods Appl. Mech. Eng. **193**, 1603 (2004).
[22] G. J. Wagner and W. K. Liu, J. Comput. Phys. **190**, 249 (2003).
[23] C. Cousins, J. Phys. C **11**, 4867 (1978).
[24] G. Zanzotto, Acta Crystallogr., Sect. A: Found. Crystallogr. **52**, 839 (1996).
[25] M. P. do Carmo, *Differential Geometry of Curves and Surfaces* (Prentice-Hall, Englewood Cliffs, NJ, 1976).
[26] F. Morgan, *Riemannian Geometry: A Beginner's Guide* (Jones and Bartlett, Boston, 1993).
[27] E. Tadmor, G. S. Smith, N. Bernstein, and E. Kaxiras, Phys. Rev. B **59**, 235 (1999).
[28] R. D. Cook, D. S. Malkus, M. E. Plesha, and R. J. Witt, *Concepts and Applications of Finite Element Analysis* (Wiley, New York, 2002).
[29] J. Tersoff, Phys. Rev. Lett. **61**, 2879 (1988).
[30] D. W. Brenner, Phys. Rev. B **42**, 9458 (1990).
[31] L. A. Girifalco, M. Hodak, and R. S. Lee, Phys. Rev. B **62**, 13104 (2000).
[32] J. Nocedal, Math. Comput. **24**, 773 (1980).
[33] D. C. Liu and J. Nocedal, Math. Program. **45**, 503 (1989).
[34] P. Poncharal, Z. L. Wang, D. Ugarte, and W. A. de Heer, Science **283**, 1513 (1999).
[35] J. R. Shewchuk, TRIANGLE, a two-dimensional quality mesh generator and Delaunay triangulator (1996). This code is linked http://www.cs.cmu.edu/~quake/triangle.html
[36] The visualizations for adaptive simulations are linked, http://me.kaist.ac.kr/~sim/4000/4300.html. Bending simulation is linked in Fig. 4 and tensile simulation linked in Fig. 5 at the site, respectively.
[37] O. A. Shenderova, D. W. Brenner, A. Omeltchenko, X. Su, and L. H. Yang, Phys. Rev. B **61**, 3877 (2000).
[38] S. L. Mielke, D. Troya, S. Zhang, J.-L. Li, S. Xiao, R. Car, R. S. Ruoff, G. C. Schatz, and T. Belytschko, Chem. Phys. Lett. **390**, 413 (2004).